J. Ocean Univ. China (Oceanic and Coastal Sea Research)
https://doi.org/10.1007/s11802-019-3877-7
ISSN 1672-5182, 2019 18 (3): 605-614
http://www.ouc.edu.cn/xbywb/
E-mail:xbywb@ouc.edu.cn

Estimation of Oceanic Heat Flux Under Sea Ice in the Arctic Ocean

LIN Long[1)], and ZHAO Jinping[1), 2), *]

1) *College of Oceanic and Atmospheric, Ocean University of China, Qingdao* 266100, *China*
2) *Key Laboratory of Physical Oceanography, Ocean University of China, Qingdao* 266100, *China*

(Received April 1, 2018; revised May 21, 2018; accepted September 18, 2018)

Abstract Oceanic heat flux (F_w) is the vertical heat flux that is transmitted to the base of sea ice. It is the main source of sea ice bottom melting. The residual method was adopted to study oceanic heat flux under sea ice. The data acquired by 28 ice mass balance buoys (IMBs) deployed over the period of 2004 to 2013 in the Arctic Ocean were used. F_w values presented striking seasonal and spatial variations. The average summer F_w values for the Canada Basin, Transpolar Drift, and Multiyear Ice area were 16.8, 7.7, and 5.9 W m^{-2}, respectively. The mean summer F_w for the whole Arctic was 10.1 W m^{-2}, which was equivalent to a bottom melt of 0.4 m. F_w showed an autumn peak in November in the presence of the near-surface temperature maximum (NSTM). The average F_w for October to December was 3.7 W m^{-2}. And the average F_w for January to March was 1.0 W m^{-2}, which was approximately one third of the average F_w in the presence of NSTM. The summer F_w was almost wholly attributed to the incident solar radiation that enters the upper ocean through leads and the open water. F_w calculated through the residual method using IMB data was compared with that calculated through the parameterization method using Autonomous Ocean Flux Buoy data. The results revealed that the F_w provided by the two methods were consistent when the sea ice concentration exceeded 70% and mixing layer temperature departure from freezing point was less than 0.15℃. Otherwise, the F_w yielded by the residual method was approximately one third smaller than that provided by the parameterization method.

Key words Arctic Ocean; oceanic heat flux; residual method; NSTM heat release

1 Introduction

Sea ice retreat in the Arctic Ocean during summers has accelerated in recent years (Parkinson and Cavalieri, 2008; Cavalieri and Parkinson, 2012; Comiso, 2012; Stroeve *et al*., 2012, 2014; Vihma, 2014). Record September minimum ice covers were observed in 2007 and 2012 (Stroeve *et al*., 2008; Parkinson and Comiso, 2013). Submarine and aerial electromagnetic surveys and satellite observations have revealed drastic reductions in ice thickness (Rothrock *et al*., 2008; Kwok and Rothrock, 2009; Kwok and Untersteiner, 2011; Laxon *et al*., 2013). Oceanic heat flux (F_w) at the ice-ocean interface is a key factor of ice mass balance and regulates ice bottom melt during melting season and ice growth during freezing season (Maykut and Untersteiner, 1971; Stanton *et al*., 2012).

Direct measurements of F_w are difficult to obtain because they require frequent, high-precision determinations of temperature, salinity, and vertical velocity in the near-surface boundary layer under drifting sea ice (McPhee, 1992; McPhee and Stanton, 1996; Peterson *et al*., 2017). A simplified parameterization method for the estimation of F_w has been developed on the basis of F_w obtained from three ice camps; in this approach, the mixed layer temperature above the freezing temperature (ΔT_f) is modulated, and the ice-ocean friction velocity (u^*) is inferred from a statistical relationship that is based on ice-drift velocity (McPhee, 1992, 2002). The parameterization method is widely used because it is easier to perform and less costly than direct measurement (McPhee *et al*., 2003; Krishfield and Perovich, 2005; Peterson *et al*., 2017).

The residual method is another indirect method for estimating time average F_w from ice temperature profiles and ablation or accretion measurements at the ice bottom (McPhee and Untersteiner, 1982; Perovich *et al*., 1989, 1997; Perovich and Elder, 2002; Lei *et al*., 2014). F_w is the residual component of conductive heat flux (F_c), specific heat flux (F_s), and latent heat flux (F_l). A large number of autonomous ice mass balance buoys (IMBs) have been deployed on the Arctic drift pack ice starting in the 21st century (Morison *et al*., 2002). These buoys measure sea ice temperature profiles with thermistor strings, and mass balances with acoustic sounders to monitor the ablation and accumulation of ice and snow at the top and bottom of the ice cover (Richter-Menge *et al*., 2006; Perovich *et al*., 2014). They transmit real-time data by satellite com-

* Corresponding author. Tel: 0086-532-66782096
E-mail: jpzhao@ouc.edu.cn

munication. In this work, the residual method and IMB data were applied to study the time average F_w in the Arctic Ocean. Moreover, the results of the residual method were compared with those of the parameterization method.

2 Data and Residual Method for Oceanic Heat Flux Calculation

IMBs were designed and deployed by the Cold Region Research and Engineering Laboratory. The name of each IMB was based on buoy deployment year and one English letter. The spacing of the thermistor in the string was 0.10 m, and the accuracy was 0.1 K. The accuracy and resolution of the acoustic sensors were 0.01 m (http://imb.erdc.dren.mil/massbal.htm). Autonomous ocean flux buoy (AOFB) data were acquired from the Ocean Turbulence Laboratory, Oceanography Department, Naval Postgraduate School. Time average temperature, salinity, and velocity under sea ice were applied in F_w calculation through the parameterization method (http://www.oc.nps.edu/~stanton/fluxbuoy/index.html). Ice-tethered profile (ITP) data were obtained from Woods Hole Oceanography Institution. Sea ice concentrations were derived from Advanced Microwave Scanning Radiometer-EOS brightness temperatures with a spacing of 6.25 km × 6.25 km (Spreen *et al.*, 2008). Daily average sea ice concentration at buoy positions was estimated by averaging the concentration value from grid points lying within circles with 100 km radii. The NCEP/NCAR atmospheric reanalysis data of daily 10 m-height wind speed, downward short wave radiation under clear skies, and cloud fraction were used to ascertain local atmospheric forcing (Kistler *et al.*, 2001). Bathymetric data were obtained from the International Bathymetric Chart of the Arctic Ocean (Jakobsson *et al.*, 2008).

Undeformed pack ice, excluding ice ridge, leads, or melt ponds, was considered as sea ice in this work. Snow-covered undeformed ice has a uniform thickness within a certain space. Ice thickness is closely related to atmospheric temperature. The changes in conductive heat flux through sea ice with atmospheric temperature results in the adjustment of sea ice thickness. The ice surface and bottom melt during the melting season, whereas the ice bottom can only grow during the freezing season. Although air temperature, surface wind, and barometric pressure change frequently, ice bottom ablation and accretion are slow processes that occur under quasiequilibrium conditions. Thus, the oceanic heat flux related to the sea ice bottom melt and growth can be determined by using the heat balance equation.

A reference layer was defined at 0.3–0.7 m above the ice base to account for the nonlinearity of the vertical ice temperature profile in the ice base layer where the temperature gradient is small (Lei *et al.*, 2014). The thermal flux at the base of the ice is entered into the following heat balance equation:

$$F_c + F_l + F_s - F_w = 0\,, \tag{1}$$

where F_w represents oceanic heat flux, F_l is equivalent latent heat flux resulting from ice freezing or melting, and F_s is specific heat flux resulting from ice warming or cooling. The sign convention is such that upward melting and warming heat flux are positive, whereas downward freezing and cooling heat flux are negative.

Conductive heat flux is given by

$$F_c = K_{\text{ice}} T_z\,, \tag{2}$$

where T_z, the vertical ice temperature gradient of the reference layer, refers to the linear trend of the temperature profile in the reference layer, and K_{ice} is sea ice thermal conductivity, which is a function of ice temperature and ice salinity (Untersteiner, 1961).

Latent heat flux is given as follows (Semtner Jr., 1976):

$$F_l = -\rho_{\text{ice}} L_{\text{ice}} \left(\frac{\mathrm{d}H_i}{\mathrm{d}t}\right)_0\,, \tag{3}$$

where L_{ice} is the latent heat of sea ice, $\left(\frac{\mathrm{d}H_i}{\mathrm{d}t}\right)_0$ is the ice growth or melting rate, ρ_{ice} is the sea ice density (917 kg m^{-3}).

Specific heat flux is given below (Semtner Jr., 1976):

$$F_s = \rho_{\text{ice}} c_s \frac{\mathrm{d}T_{\text{ice}}}{\mathrm{d}t} \Delta H\,, \tag{4}$$

where $\frac{\mathrm{d}T_{\text{ice}}}{\mathrm{d}t}$ is the average temperature variation rate of the reference layer, ΔH is the thickness of the reference layer, and c_s is the specific heat of the sea ice and is a function of sea ice temperature and salinity (Yen *et al.*, 1991).

Eq. (1) shows that four components of heat exist at the ice-ocean interface: conductive heat through sea ice, specific heat from sea ice warming or cooling, latent heat from bottom melting or freezing, and oceanic heat from the underlying mixing layer. Thus, F_w can be estimated from the other three terms (F_c, F_l, and F_s).

3 Oceanic Heat Flux Under Arctic Sea Ice

As Eq. (1) shows, F_w can be easily estimated as long as the sea ice temperature profiles and bottom growth or melting rate can be obtained through the support of IMBs. Each IMB is fixed on the ice floe. IMBs are continuously tracked and provide an ideal platform for applying the residual method for the investigation of the time average F_w.

The accuracy of IMB data can meet the requirements of the residual method. Abnormal data caused by mast slipping or slanting and thermistor unit malfunction must be eliminated. A total of 28 IMBs with good data quality were selected for the investigation of the time average F_w in the Arctic Ocean. These IMBs were mainly distributed in the Canada Basin, Polar Drift, and the Multiyear Ice area. The buoy observation time ranged from 2004 to 2015. Each buoy drifting trajectory and observation time are shown in Fig.1.

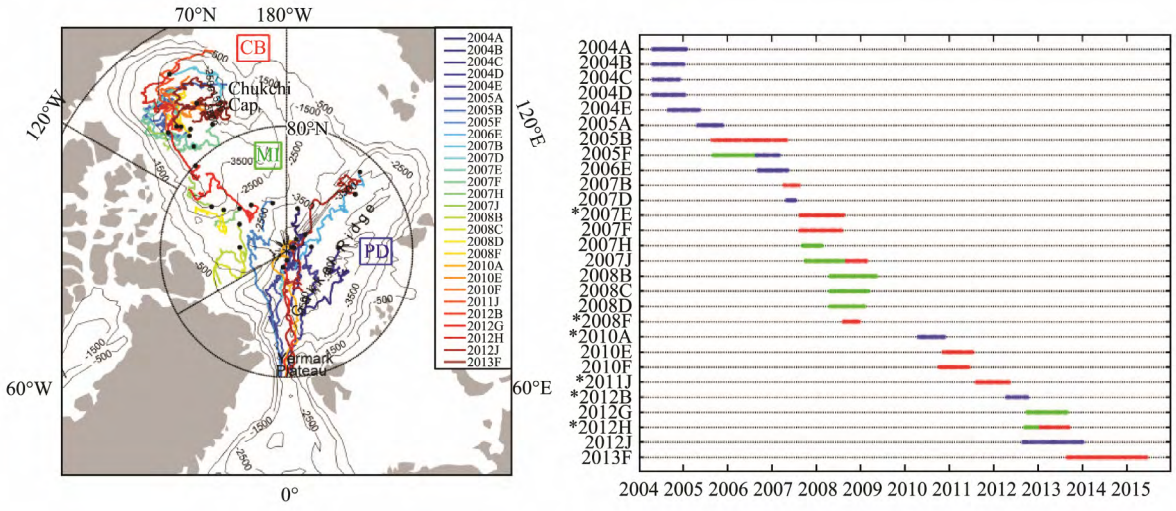

Fig.1 28 IMB information. Left panel is buoy drifting trajectory. Black dots represent the initial positions of the buoys. The Canada Basin (CB), Polar Drift (PD), and Multiyear Ice (MI) area are distinguished by dashed lines. Right panel is buoy observation time. Red represents the CB; blue represents PD; and green represents the MI. '*' represents the buoy co-located with AOFB.

Given that sea ice bottom melt and growth are slow processes, the major difficulty encountered when using the residual method lies in the precise determination of the amount of ice melt or growth. The residual method works best when averaging over long time intervals (Perovich *et al.*, 1989; Perovich and Elder, 2002). Abnormal data were first eliminated to guarantee the accuracy of F_w. Moving quadratic fitting was then applied to the daily mean bottom position for 30 d and selected 10-day intervals. The process of 2010F's bottom position is illustrated in Fig.2.

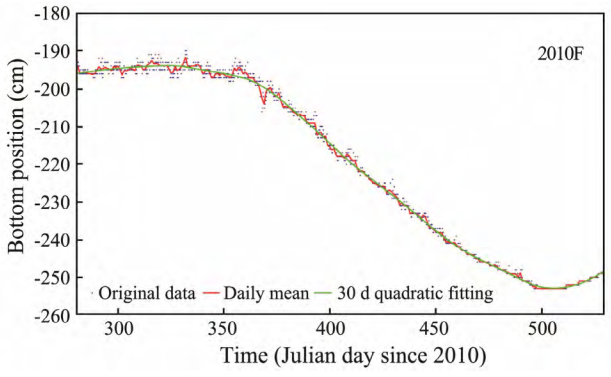

Fig.2 Bottom position of IMB 2010F. Blue dots represent the data for the original bottom position of the IMB. The red line is the daily mean. The green line is the result after 30-day quadratic fitting.

Given that the reference layer was near the base of the sea ice, the temporal temperature variation in the reference layer was small, and the specific heat flux for the whole year was less than 1 W m^{-2}. Thus, specific heat flux was ignored and not shown in Fig.3. The warming of the ice column and underlying mixing layer by incident solar radiation during melting season resulted in the formation of a small gradient in the reference layer and high oceanic heat content. F_c was always less than 5 W m^{-2} and even became negative, whereas F_w was high and frequently exceeded 20 W m^{-2}, which was comparable with the latent heat of bottom melting F_l. Thus, almost all of the oceanic heat contributed to bottom melting. The heat balance in the ice-ocean interface was dominated by oceanic heat flux and conductive heat flux. The reduction in air temperature during freezing season caused the formation of a large temperature gradient that, in turn, resulted in large F_c values. F_c varied within a range of 10 to 20 W m^{-2} and was almost equal to the latent heat of sea ice fusion. The derived F_w decreased gradually to near 0 W m^{-2} as the melting season progressed to the freezing season. The heat balance in the ice-ocean interface was dominated by conductive heat flux and latent heat flux.

Oceanic heat flux shows strong seasonal dependence as illustrated in Fig.4. Ice concentration decreased, and the incident solar radiation absorbed by the upper ocean increased and contributed to bottom melting at the beginning of the melting season. The average F_w for summer time (June to September) was 10.1 W m^{-2}. The F_w values provided by some IMBs even exceeded 40 W m^{-2} in July and August and were equivalent to a melt of 1.5 cm per day. During freezing season, solar radiation disappeared, and oceanic heat originated from the inner ocean through turbulent mixing. The average F_w from October to May was 2.0 W m^{-2}, which was consistent with previous model results (Maykut and Untersteiner, 1971). The annual average F_w for the total Arctic Ocean was 4.7 W m^{-2}. This value was comparable with the values observed in 1975 during AIDJEX (Maykut and McPhee, 1995) and was half of those observed in 1997 during SHEBA (Perovich and Elder, 2002). Seasonal variations in different areas were consistent. The summer time average F_w in the CB was the largest and was approximately 16.8 W m^{-2}. The F_w in the Po-

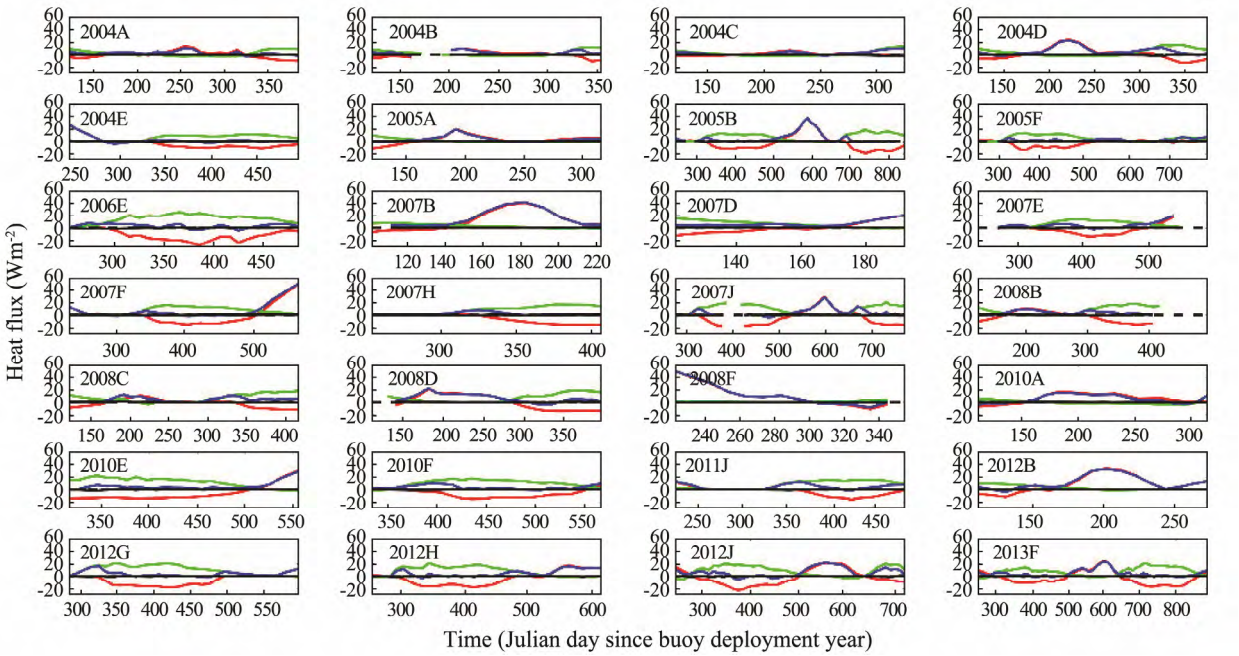

Fig.3 Heat balance of 28 IMBs. Blue lines represent the oceanic heat flux F_w, green lines represent conductive heat flux F_c, red lines represent latent heat flux F_l, and the black dashed line is the 0 reference line. Time is the Julian day of the buoy deployment year.

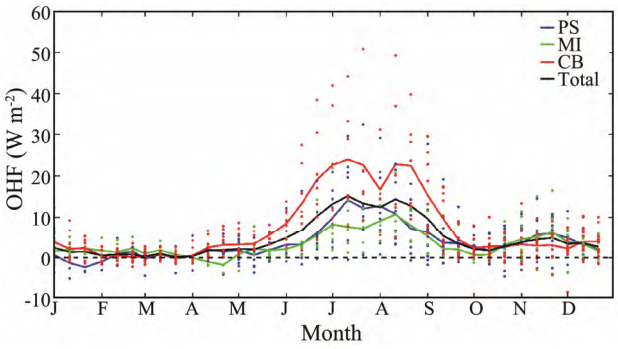

Fig.4 Seasonal variation in oceanic heat flux. Red dots and lines represent CB, blue dots and lines represent PD, green dots and lines represent MI, and the black line represents the total Arctic.

lar Drift was half of that in the CB and was approximately 7.7 W m^{-2}. The F_w in the Multiyear Ice area was the smallest and was 5.9 W m^{-2}. Incident solar radiation enters the upper ocean through leads or thin ice and is rapidly mixed and stored in the upper ocean. Over the course of the summer season, the majority of this absorbed heat is transported to the base of the ice cover by oceanic heat flux. Oceanic heat flux is determined by the heat content of the upper ocean and turbulent mixing in the boundary layer (Mcphee, 1992). The net incident solar radiation that enters the upper ocean through leads or open water was calculated by ignoring penetrative heat through sea ice and by using the following equation (Stanton *et al.*, 2012):

$$nSW = SW(1-0.25c^3)(1-\alpha_w)(1-C_i)\,, \qquad (5)$$

where SW is the downward shortwave flux at the top of the atmosphere; c is the cloud fraction; α_w is the albedo of open water and leads (taken as 0.07) (Pegau and Paulson, 2001); and $(1–C_i)$ is the open water fraction, where C_i the local ice concentration. The local conditions of four IMBs are presented in Fig.5. These conditions included sea ice concentration, bathymetry, wind speed, ice drifting speed, and net solar radiation. Summer sea ice concentration was less than 60%, and the net short wave flux was consistent with the temporal variation in the derived oceanic heat flux F_w for IMB 2005B and IMB 2013F (Figs.5a and 5b). Thus, the observed oceanic heat flux during melting season was almost wholly contributed by incident solar radiation. Rapid drifting can strengthen turbulent mixing under sea ice and facilitate the release of oceanic heat (Rampal *et al.*, 2009). In IMB 2004D (Fig.5c), the abrupt increase in ice drifting speed from 5 to 20 cm s^{-1} during autumn resulted in strong turbulent mixing under sea ice and efficient oceanic heat release. The maximum F_w reached nearly 10 W m^{-2} and was far greater than the autumn average. IMB 2008C escaped from Beaufort Gyre to the Alaskan coastal current during a storm event in January 2009. Oceanic heat flux during winter was approximately 5.0 W m^{-2} (Fig.5d) but is usually only approximately 1.0 W m^{-2}. Similar results have been obtained for the Yermark Plateau, north of Svalbard (McPhee *et al.*, 2003), and Chukchi Cap (Shaw *et al.*, 2009). Consequently, oceanic heat flux during melting season is determined by the incident solar radiation that enters the upper ocean through the inner ocean and that during the freezing season is determined by interference by bathymetry and drifting speed.

Two cases for the derivation of F_w for the freezing season through the residual method exist. The F_w values of

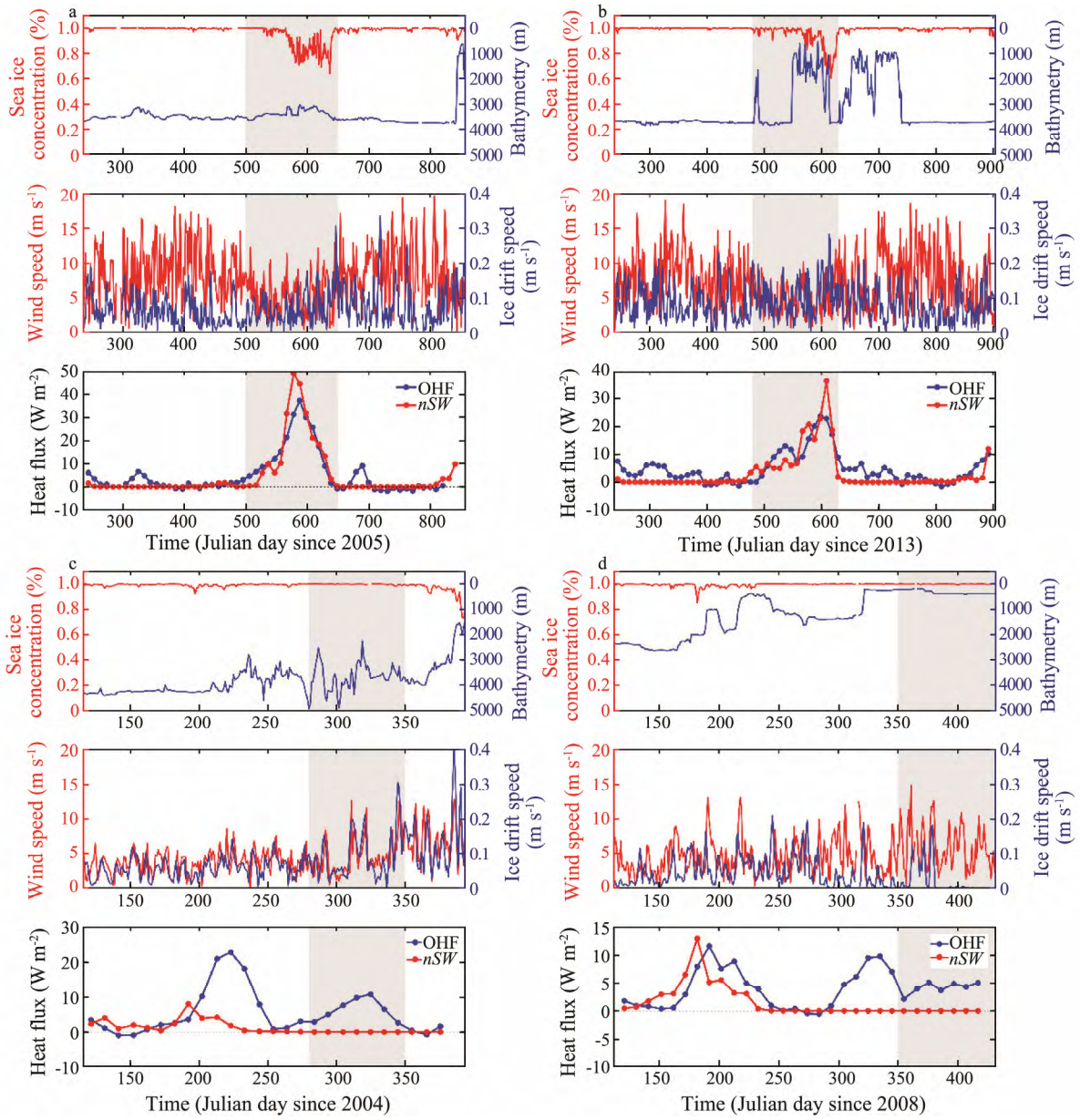

Fig.5 Influential factors of oceanic heat flux. a, b, c, and d represent the local conditions of IMB 2005B, 2013F, 2004D, and 2008C, respectively. These conditions include sea ice concentration, bathymetry, wind speed, drifting speed, net shortwave flux, and derived F_w.

12 IMBs for the freezing season were steady and the average F_w was approximately 1.6 W m^{-2}, whereas those of 16 other IMBs peaked in autumn. F_w decreased in September with the decrease in solar radiation. After the disappearance of solar radiation, air temperature was lower than the sea ice freezing point, and the ice column and underlying mixing layer began to cool. F_w at the ice-ocean interface originated from the heat deposited in the mixing layer and tended to decrease. During summer time, a portion of solar radiation is stored under the mixing layer and is trapped by a strong seasonal halocline, which is designated as the near-surface temperature maximum (NSTM) (Jackson *et al.*, 2010; Zhao and Cao, 2011). The heat stored in the NSTM is released upward only when the mixing layer reaches the top of the NSTM (Jackson *et al.*, 2012). The heat in the NSTM was gradually released as the mixing layer deepened through convection and brine rejection during the freezing season. F_w peaked in November, and the peak F_w value averaged over 10 days was 6.4 W m^{-2}. Then, F_w decreased again and stabilized. The time average F_w for October to December was 3.7 W m^{-2} and was far more than that for January to March (1.0 W m^{-2}).

The deepening of the mixing layer caused by convective mixing and shear-driven mixing is a slow process as shown in Fig.6a, except for episodic events. Winter storms with speeds of at least 10 m s^{-1} can cause the abrupt erosion of the summer halocline and explosive heat release from the NSTM to the ice-ocean interface (Jackson *et al.*, 2012; Timmermans, 2015). Figs.6b and 6c illustrate the NSTM temperature and salinity profiles observed during storm events. The mixing layer depth of the two buoys increased by nearly 4 m in 1 day. The sea ice bottom melted

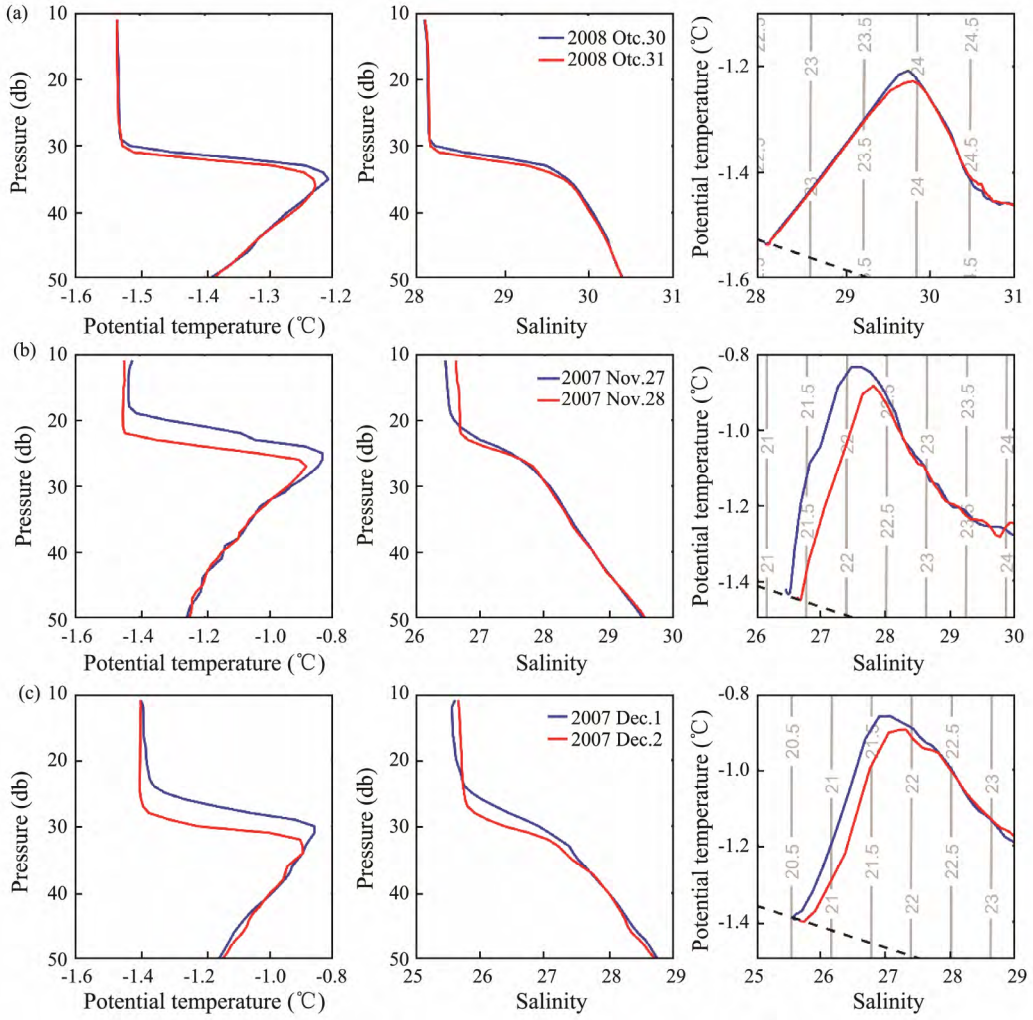

Fig.6 (left column) Potential temperature (℃) and (middle column) salinity profiles and (right column) corresponding potential temperature-salinity (θ-S) plots. Solid black lines are the contours of potential density relative to the surface, and the dashed-dotted line is the freezing line. (a) ITP11 profiles colocated with 2007J; (b) ITP 13 profiles colocated with 2007F; and (c) ITP 18 profiles colocated with 2007E.

during freezing season when F_w exceeded 95 W m^{-2}.

A shown in Fig.7, the summer oceanic heat flux shows significant spatial variation. The largest summer F_w occurred in the south of the CB and Beaufort Sea, followed by that in the south of the Eurasia Basin. The F_w in the central Arctic and Multiyear Ice areas was the smallest. As mentioned above, the summer oceanic heat flux is determined by the incident solar radiation that enters the upper ocean. Sea ice in the southern CB and Beaufort Sea was dominated by easily melting 1-year ice. High summer solar radiation at low latitudes decreased sea ice concentration, prolonged melting season, and drastically increased heat deposition in the upper ocean. Summer F_w was usually larger than 15 W m^{-2} and even exceeded 40 W m^{-2} in some regions in July and August. Sea ice in the central Arctic and Multiyear Ice area, however, was dominated by thick multiyear ice. The high sea ice concentration at high latitudes shortened the melting season, limited the entry of incident solar radiation into the upper ocean, and decreased oceanic heat flux. Summer F_w was commonly less than 10 W m^{-2}. The F_w values for some individual buoys, however, exceeded 15 W m^{-2}. The southern part of the Eurasian Basin is close to the Gakkel Ridge and Yermark Plateau, which is topographically complex. Under the influence of the warm inflow from the North Atlantic, summer F_w usually exceeded 15 W m^{-2} and may even exceed 30 W m^{-2} at the end of July.

4 Comparison of the Oceanic Heat Flux Value Calculated Through the Residual Method with that Calculated Through the Parameterization Method

True oceanic heat flux remains mysterious. Identifying the best method for determining oceanic heat flux is difficult because methods for oceanic heat flux determination are based on different theories. However, these methods must be compared with each other to identify their differences and understand their practicability. The residual method for oceanic heat flux calculation is based on the heat balance at the ice-ocean interface and sea ice parameters acquired from IMBs, whereas the parameteriza-

tion method is based on ocean parameters acquired from AOFBs (Shaw *et al.*, 2008). Six of the 28 IMBs were deployed on the same ice with AOFBs (Fig.1b). The parameterization method is described as follows:

$$F_w = \rho_{sw} c_p C_H u_{*0} \delta T \,, \tag{6}$$

where ρ_{sw} is the sea water density ($1028\,\mathrm{kg\,m^{-3}}$); c_p is the specific heat of seawater ($3980\,\mathrm{J\,kg^{-1}}$); C_H is a bulk heat transfer coefficient (0.0057; McPhee, 1992); u_{*0} is the interface friction velocity as described in Eq. (7); and $\delta T = T_{ml} - T_f(S_{ml})$, where T_{ml} and S_{ml} are the temperature and salinity of the mixing layer, respectively. u_{*0} is calculated by using the Rossby similarity theory

$$\frac{V_0}{u_{*0}} = \frac{1}{\kappa}\left(\ln\frac{u_{*0}}{fz_0} - A + iB\right), \tag{7}$$

where V_0 is the ice velocity relative to the surface geostrophic flow measured by the AOFB; κ is von Karman's constant (0.4); f is the Coriolis parameter; z_0 is the hydraulic roughness length of the underside of the ice (0.1 m; Stanton *et al.*, 2012); and A and B are similarity constants with values of 2.21 and 1.91, respectively.

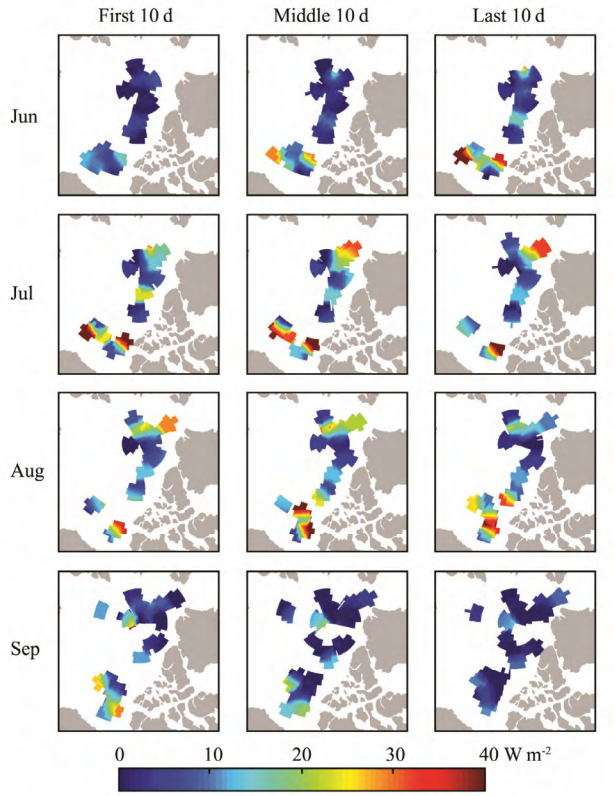

Fig.7 Spatial variation in oceanic heat flux during melting season.

The comparison of the oceanic heat flux value calculated by these two methods is presented in Fig.8. IMB 2010A survived a whole summer. The summer sea ice concentration along the drifting trajectory was always larger than 70%, and the deviation of the mixing layer temperature from the freezing point was less than 0.15℃. Meanwhile, the ice drifting speed and friction velocity in the ice-ocean interface were smaller than those in other areas with a high concentration. The F_w values provided by the two methods were comparable and highly consistent. When the summer sea ice concentration was less than 70%, such as that observed during the beginning of the deployment of IMB 2008F and 2011J and the end of the deployment of 2007E, 2012B, and 2012H, the deviation of the mixing layer temperature from the freezing point usually exceeded 0.15℃, and the ice drifting speed and friction velocity were faster than those at IMB 2010A. The F_w provided by the residual method was one third smaller than that provided by the parameterization method. The underlying mixing layer temperature was maintained at the freezing point during the freezing season. Given this condition, the F_w value provided by the parameterization method was almost 0. Thus, the parameterization method cannot reflect heat release from the NSTM during freezing season as represented by 2011J and 2012H. Given that sea ice bottom melting and growth are slow processes, the F_w yielded by the residual method cannot reflect the high-frequency variation in turbulent mixing intensity caused by drift speed changes. Both of these two methods have their advantages and disadvantages in the calculation of oceanic heat flux. Determining which method provides values that are close to true values remain difficult given the lack of direct oceanic heat flux measurements.

5 Discussion and Conclusions

Oceanic heat flux under sea ice is the vertical heat flux transmitted to the base of sea ice. The direct measurements of oceanic heat flux turbulence are difficult to obtain. The temporally averaged values of oceanic heat flux can be determined from the simple measurements of ice temperatures and mass balance. IMB data were applied to derive oceanic heat flux values through the residual method. The residual method was compared with the parameterization method. The potential error in heat flux estimation by the residual method originated from any uncertainty in ice salinity, ice temperature, and bottom position. Sea ice salinity ranged from 4 to 12 (Nakawo and Sinha, 1981) and had a potential error of $\pm 1.4\,\mathrm{W\,m^{-2}}$ for F_c, $\pm 3.3\times 10^{-3}\,\mathrm{W\,m^{-2}}$ for F_s and $\pm 1.9\,\mathrm{W\,m^{-2}}$ for F_l. The thermistor accuracy of ± 0.1 K corresponded to an error of $\pm 0.5\,\mathrm{W\,m^{-2}}$ for F_c and $\pm 0.07\,\mathrm{W\,m^{-2}}$ for F_s. The largest uncertainty was contributed by ice bottom position. The accuracy of ±0.01 m for the ice thickness measurement corresponded to a potential error of $2.8\,\mathrm{W\,m^{-2}}$ for F_l over a 10-day interval.

Heat balance in the ice-ocean interface is dominated by oceanic heat flux and latent heat flux from the melting of the sea ice bottom during the melting season and by conductive heat flux through sea ice and latent heat flux from bottom growth during the freezing season. The residual method reflects this relationship well.

The seasonal variation in oceanic heat flux peaked twice: once in the summer and once in autumn. In addition to warm inflow, most of the oceanic heat during the melting season originated from incident solar radiation, which

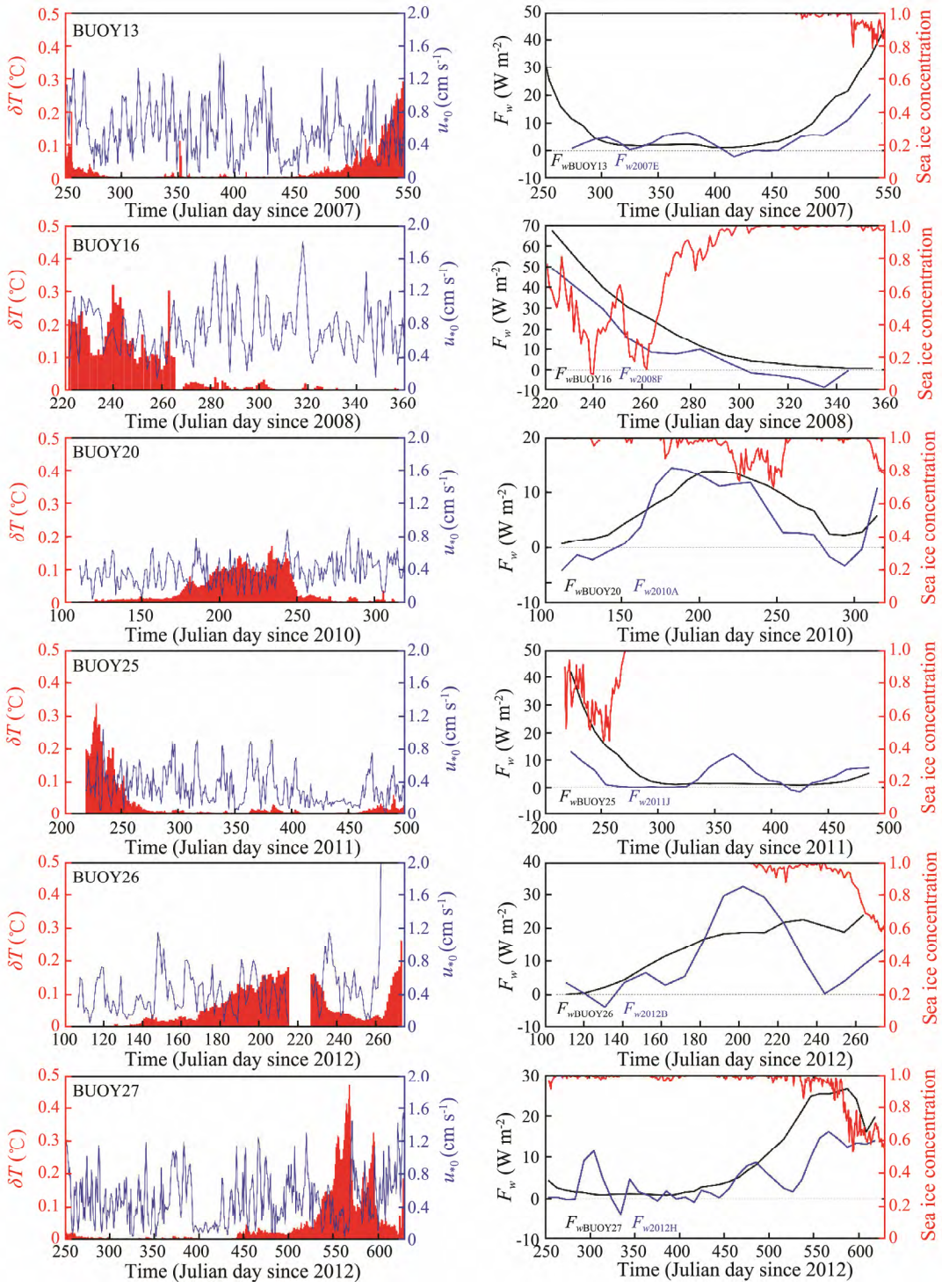

Fig.8 Comparison of F_w values provided by the residual method and parameterization method. The left column shows the deviation of the mixing layer temperature from the freezing temperature δT (red) and interface friction speed u_{*0} (blue). The right column shows the sea ice concentration along the drifting trajectory (red) and the F_w values derived through the residual method (blue) and parameterization method (black).

resulted in the summer peak of oceanic heat flux. The average F_w for the freezing season was approximately 2.0 $\mathrm{W\,m^{-2}}$ and can be divided into two cases. In the first case, the NSTM was absent, and oceanic heat flux originated from the turbulent mixing of the inner ocean. In this case, the F_w for the entirety of the freezing season was small, stable, and approximately 1.6 $\mathrm{W\,m^{-2}}$. In the other case, the NSTM existed under the mixing layer, and the freezing season could be divided into two stages. The first stage lasted from October to December. During this stage, oceanic heat basically originated from the NSTM. Convective mixing and brine rejection during freezing weakened the summer halocline and resulted in gradual heat release from the NSTM. The time average F_w was 3.7 $\mathrm{W\,m^{-2}}$. Episodic events could cause the abrupt erosion of the summer halocline. The extremely high oceanic heat flux from the

NSTM during storm events can even melt ice during the freezing season. The second stage lasted from January to March. Oceanic heat flux originated from the turbulent mixing of the inner ocean. The average F_w was $1.0\,\mathrm{W\,m^{-2}}$ and was one third of that of NSTM. It may be attributed to phytoplankton blooms during the summer (Manizza *et al*., 2005).

Six IMBs were deployed on the same ice as AOFB. The results for the summer oceanic heat flux provided by the residual method and parameterization method can be divided into two cases. The friction velocity was small and the results for F_w obtained through the residual method and the parameterization method were comparable and highly consistent when sea ice concentration was higher than 70% and the deviation of the mixing layer temperature from the freezing point was less than 0.15℃. By contrast, the F_w value provided by the residual method was one third smaller than that provided by the parameterization method when the sea ice concentration was less than 70% and the deviation of the mixing layer temperature from the freezing point was higher than 0.15℃. Nevertheless, definitively identifying the superior method for the determination of oceanic heat flux remains difficult because of the lack of direct F_w measurements. The F_w yielded by the parameterization method was larger than that yielded by the residual method because AOFBs measured temperatures at 7 m under the ice base. During freezing season, the mixing layer temperature was maintained at the freezing point, and the F_w yielded by the parameterization method was near zero. However, the F_w provided by the residual method could still reflect heat release from the NSTM and the intensification of turbulent mixing. Consequently, the residual method relies on the heat balance at the ice-ocean interface in sea ice melting or freezing with clear physical basis, and it can be applied for any season. The oceanic heat flux provided by the residual method is reliable.

The IMB data are the basis for calculating the oceanic heat flux under sea ice using residual method. The temporal and spatial resolution remains low given the limited number of mass balance buoys. The deployment of additional IMBs in the future can strengthen the understanding of the variations in oceanic heat flux in the Arctic Ocean.

Acknowledgements

This study was supported by the National Basic Research Program of China (No. 2015CB953900), the National Natural Science Foundation of China (No. 41330960), and the National Key Research and Development Plan (No. 2016YFC1402705)

References

Cavalieri, D. J., and Parkinson, C. L., 2012. Arctic sea ice variability and trends, 1979–2010. *The Cryosphere*, **6**: 881-889, DOI: 10.5194/tc-6-881-2012.

Comiso, J. C., 2012. Large decadal decline of the Arctic multiyear ice cover. *Journal of Climate*, **25** (4): 1176-1193.

Jackson, J., Carmack, E., McLaughlin, F., Allen, S. E., and Ingram, R., 2010. Identification, characterization, and change of the near-surface temperature maximum in the Canada Basin, 1993–2008. *Journal of Geophysical Research: Oceans*, **115**: C05021, DOI:10.1029/2009JC005265.

Jackson, J. M., Williams, W. J., and Carmack, E. C., 2012. Winter sea-ice melt in the Canada Basin, Arctic Ocean. *Geophysical Research Letters*, **39** (3): L03603.

Jakobsson, M., Macnab, R., Mayer, L., Anderson, R., Edwards, M., Hatzky, J., Schenke, H. W., and Johnson, P., 2008. An improved bathymetric portrayal of the Arctic Ocean: Implications for ocean modeling and geological, geophysical and oceanographic analyses. *Geophysical Research Letters*, **35**: L07602, DOI: 10.1029/2008GL033520.

Kistler, R., Kalnay, E., Collins, W., Saha, S., White, G., Woollen, J., Chelliah, M., Ebisuzaki, W., Kanamitsu, M., Kousky, V., Dool, H., Jenne, R., and Fiorino, M., 2001. The NCEP-NCAR 50-year reanalysis: Monthly means CD-ROM and documentation. *Bulletin of the American Meteorological Society*, **82** (2): 247-268.

Krishfield, R. A., and Perovich, D. K., 2005. Spatial and temporal variability of oceanic heat flux to the Arctic ice pack. *Journal of Geophysical Research: Oceans*, **110** (C7): C07021.

Kwok, R., and Rothrock, D. A., 2009. Decline in Arctic sea ice thickness from submarine and ICESat records: 1958–2008. *Geophysical Research Letters*, **36** (15): L15501.

Kwok, R., and Untersteiner, N., 2011. The thinning of Arctic sea ice. *Physics Today*, **64**: 36-41.

Laxon, S. W., Giles, K. A., Ridout, A. L., Wingham, D. J., Willatt, R., Cullen, R., Kwok, R., Schweiger, A., Zhang, J., Hass, C., Hendricks, S., Krishfield, R., Kurtz, N., Farrell, S., and Davidson, M., 2013. CryoSat-2 estimates of Arctic sea ice thickness and volume. *Geophysical Research Letters*, **40** (4): 732-737.

Lei, R. B., Li, N., Heil, P., Cheng, B., Zhang, Z., and Sun, B., 2014. Multiyear sea ice thermal regimes and oceanic heat flux derived from an ice mass balance buoy in the Arctic Ocean. *Journal of Geophysical Research: Oceans*, **119**: 537-547.

Manizza, M., Le Quéré, C., Watson, A. J., and Buitenhuis, E. T., 2005. Bio-optical feedbacks among phytoplankton, upper ocean physics and sea-ice in a global model. *Geophysical Research Letters*, **32**: L05603, DOI:10.1029/2004GL020778.

Maykut, G. A., and McPhee, M. G., 1995. Solar heating of the Arctic mixed layer. *Journal of Geophysical Research: Oceans*, **100** (C12): 24691-24703.

Maykut, G. A., and Untersteiner, N., 1971. Some results from a time-dependent thermodynamic model of sea ice. *Journal of Geophysical Research*, **76** (6): 1550-1575, DOI:10.1029/JC076i006p01550.

McPhee, M. G., 1992. Turbulent heat-flux in the upper ocean under sea ice. *Journal of Geophysical Research*, **97** (C4): 5365-5379.

McPhee, M. G., 2002. Turbulent stress at the ice/ocean interface and bottom surface hydraulic roughness during the SHEBA drift. *Journal of Geophysical Research*, **107** (C10): 8037, DOI: 10.1029/2000JC000633.

McPhee, M. G., and Stanton, T. P., 1996. Turbulence in the statically unstable oceanic boundary layer under Arctic leads. *Journal of Geophysical Research*, **101** (C3): 6409-6428.

McPhee, M. G., and Untersteiner, N., 1982. Using sea ice to measure vertical heat flux in the ocean. *Journal of Geophysical Research*, **87**: 2071-2074.

McPhee, M. G., Kikuchi, T., Morison, J. H., and Stanton, T. P.,

2003. Ocean-to-ice heat flux at the north pole environmental observatory. *Geophysical Research Letters*, **30** (24): 2274, DOI: 10.1029/2003GL018580.

Morison, J. A., Aagaard, K., Falkner, K. K., Hatakeyama, K., Moritz, R., and Overland, J. E., 2002. North pole environmental observatory delivers early results. *EOS*, **83** (33): 360-361.

Nakawo, M., and Sinha, N. K., 1981. Growth rate and salinity profile of first-year sea ice in the high Arctic. *Journal of Glaciology*, **27** (96): 315-330.

Parkinson, C. L., and Cavalierieri, D. J., 2008. Arctic sea ice variability and trends, 1979–2006. *Journal of Geophysical Research*, **113**: C07003, DOI: 10.1029/2007JC004558.

Parkinson, C. L., and Comiso, J. C., 2013. On the 2012 record low Arctic sea ice cover: Combined impact of preconditioning and an August storm. *Geophysical Research Letters*, **40**: (7): 1356-1361.

Pegau, W. S., and Paulson, C. A., 2001. The albedo of Arctic leads in summer. *Annals of Glaciology*, **33**: 221-224.

Perovich, D. K., and Elder, B., 2002. Estimates of ocean heat flux at SHEBA. *Geophysical Research Letters*, **29** (9): 1344, DOI: 10.1029/2001GL014171.

Perovich, D. K., Elder, B. C., and Richter-Menge, J. A., 1997. Observations of the annual cycle of sea ice temperature and mass balance. *Geophysical research letters*, **24** (5): 555-558.

Perovich, D. K., Richter-Menge, J., Polashenski, C., Elder, B., Arbetter, T., and Brennick, O., 2014. Sea ice mass balance observations from the north pole environmental observatory. *Geophysical Research Letters*, **41**: 2019-2025.

Perovich, D. K., Tucker, W. B., and Krishfield, R. A., 1989. Oceanic heat flux in the Fram Strait measured by a drifting buoy. *Geophysical Research Letters*, **16** (9): 995-998.

Peterson, A. K., Fer, I., McPhee, M. G., and Randelhoff, A., 2017. Turbulent heat and momentum fluxes in the upper ocean under Arctic sea ice. *Journal of Geophysical Research: Oceans*, **122**: 1439-1456, DOI: 10.1002/2016JC012283.

Rampal, P., Weiss, J., and Marsan, D., 2009. Positive trend in the mean speed and deformation rate of Arctic sea ice, 1979–2007. *Journal of Geophysical Research*, **114**: C05013, DOI: 10.1029/2008JC005066.

Richter-Menge, J. A., Perovich, D. K., Elder, B. C., Claffey, K., Rigor, I., and Ortmeyer, M., 2006. Ice mass balance buoys: A tool for measuring and attributing changes in the thickness of the Arctic sea-ice cover. *Annals of Glaciology*, **44**: 205-210.

Rothrock, D. A., Percival, D. B., and Wensnahan, M., 2008. The decline in arctic sea-ice thickness: Separating the spatial, annual, and interannual variability in a quarter century of submarine data. *Journal of Geophysical Research: Oceans*, **113** (C5): C05003.

Semtner Jr., A. J., 1976. A model for the thermodynamic growth of sea ice in numerical investigations of climate. *Journal of Physical Oceanography*, **6** (3): 379-389.

Shaw, W. J., Stanton, T. P., and McPhee, M. G., 2008. Estimates of surface roughness length in heterogeneous under-ice boundary layers, *Journal of Geophysical Research: Oceans*, **113**: C08030, DOI: 10.1029/2007JC004550.

Shaw, W. J., Stanton, T. P., McPhee, M. G., Morison, J. H., and Martinson, D. G., 2009. Role of the upper ocean in the energy budget of Arctic sea ice during SHEBA. *Journal of Geophysical Research: Oceans*, **114**: C06012.

Spreen, G., Kaleschke, L., and Heygster, G., 2008. Sea ice remote sensing using AMSR-E 89 GHz channels. *Journal of Geophysical Research*, **113**: C02S03, DOI: 10.1029/2005JC003384.

Stanton, T. P., Shaw, W. J., and Hutchings, J. K., 2012. Observational study of relationships between incoming radiation, open water fraction, and ocean-to-ice heat flux in the Transpolar Drift: 2002–2010. *Journal of Geophysical Research*, **117**: C07005, DOI: 10.1029/2011JC007871.

Stroeve, J. C., Kattsov, V., Barrett, A., Serreze, M., Pavlova, T., Holland, M., and Meier, W. N., 2012. Trends in Arctic sea ice extent from CMIP5, CMIP3 and observations. *Geophysical Research Letters*, **39**: L16502, DOI: 10.1029/2012GL052676.

Stroeve, J. C., Markus, T., Boisvert, L., Miller, J., and Barrett, A., 2014. Changes in Arctic melt season and implications forsea ice loss. *Geophysical Research Letters*, **41**: 1216-1225, DOI: 10.1 002/2013GL058951.

Stroeve, J., Serreze, M., Drobot, S., Gearheard, S., Holland, M., Maslanik, J., and Scambos, T., 2008. Arctic sea ice extent plummets in 2007. *Eos, Transactions American Geophysical Union*, **89** (2): 13-14.

Timmermans, M. L., 2015. The impact of stored solar heat on Arctic sea ice growth. *Geophysical Research Letters*, **42**: 6399-6406, DOI: 10.1002/2015GL064541.

Untersteiner, N., 1961. On the mass and heat budget of Arctic sea ice. *Archiv für Meteorologie, Geophysik und Bioklimatologie, Serie A*, **12** (2): 151-182.

Vihma, T., 2014. Effects of Arctic sea ice decline on weather and climate: A Review. *Surveys in Geophysics*, **35**: 1175-1214, DOI: 10.1007/s10712-014-9284-0.

Yen, Y. C., Cheng, K. C., and Fukusako, S., 1991. Review of intrinsic thermophysical properties of snow, ice, sea ice, and frost. *Proceedings of the 3rd International Symposium on Cold Regions Heat Transfer*. Fairbanks, 187-218.

Zhao, J., and Cao, Y., 2011. Summer water temperature structures in upper Canada Basin and their interannual variation. *Advances in Polar Science*, **22** (4): 223-234.

(Edited by Chen Wenwen)